Carbon 114 (2017) 642–648

Contents lists available at ScienceDirect

Carbon

journal homepage: www.elsevier.com/locate/carbon

Exchange bias in graphitic C/Co composites

Hua-Shu Hsu [a, *], Yu-Ying Chang [a], Yi-Ying Chin [b, **], Hong-Ji Lin [b], Chien-Te Chen [b], Shih-Jye Sun [c, ***], Sergey M. Zharkov [d, e], Chun-Rong Lin [a], Sergey G. Ovchinnikov [d, e]

[a] Department of Applied Physics, National Pingtung University, 4-18, Minsheng Road, Pingtung, 90044, Taiwan, ROC
[b] National Synchrotron Radiation Research Center, 101 Hsin-Ann Road, Hsinchu, 30013, Taiwan, ROC
[c] Department of Applied Physics, National University of Kaohsiung, 700, Kaohsiung University Road, Kaohsiung, 81148, Taiwan, ROC
[d] Kirensky Institute of Physics, SB RAS, Akademgorodok 50, Bld. 38, Krasnoyarsk, 660036, Russia
[e] Siberian Federal University, 79 Svobodny pr., Krasnoyarsk, 660041, Russia

ARTICLE INFO

Article history:
Received 2 October 2016
Received in revised form
13 December 2016
Accepted 21 December 2016
Available online 24 December 2016

ABSTRACT

The exchange bias (EB) effect, which is the shift of the hysteresis loop of a ferromagnet in direct contact with an antiferromagnet, is highly advantageous for the development of spintronics applications. Carbon (C) has been considered as a potential material in next generation electronics production as well as spintronics devices beyond silicon. Here we show experimental evidence for an EB in C/Co composites. The significant EB needs thermal annealing to occur. X-ray absorption spectra and transmission electron microscopy data of these samples reveal that Co carbides in as grown samples decompose and form graphitic C/Co interfaces after annealing. Using x-ray magnetic circular dichroism we have detected the C spins that are responsible for the EB. These results inspire a theoretical model to investigate the magnetic interactions in graphitic C/Co interfaces and interpret the observed results.

1. Introduction

When materials with antiferromagnetic (AFM) and ferromagnetic (FM) interfaces are cooled through the Neel temperature (T_N) of the AFM layer (with the Curie temperature, T_C, of the FM larger than T_N), exchange coupling between AFM and FM materials causes an exchange bias (EB) effect from a unidirectional anisotropy forced on the FM layer [1–3]. It means when the magnetization of an FM layer is pinned into a well-defined direction by an AFM, its hysteresis loop will exhibit a horizontal shift. The EB effect plays an important role for spintronics applications such as magnetic random-access memory and spin valves [4,5]. In recent, carbon (C) based spintronics materials and devices have been extensively studied both experimentally and theoretically [6–16]. Moreover, the interfacial effects between FM transitional metals (TMs) and C-based materials have attracted considerable attention. The magnetic proximity effects in C/TM systems have also been evidenced by using x-ray magnetic circular dichroism (XMCD), ultraviolet–visible (UV–VIS) magnetic circular dichroism MCD, and polarized neutron reflectivity by some research groups, including ours [17–21]. The origin of both the EB phenomenon and the magnetic proximity effect is an interlayer exchange coupling. As a result, these two novel phenomena may occur simultaneously in a single system. However, sometimes one may be present, while the other remains absent [22]; such situations motivate researchers to seek an EB effect in C/TM structures. However, this effect has never been reported in C/TM structures.

Amorphous carbon (*a*-C) is an amorphous semiconductor with a mixture of sp^2 and sp^3 hybridizations [23]. Large *a*-C films can be grown easily for wafer-scale fabrication and they are compatible with various substrates. However, the modulation of the properties of *a*-C can be challenging. Practitioners understand that, with respect to the C microstructure, the presence of a metal promotes the formation of sp^2-bonded C nanostructures by metal-contact-induced graphitization following suitable annealing [24–28]. These metals have a large solid solubility of the elemental component of the *a*-C: the phase diagram often consists of a eutectic system. The atoms of the nonordered C become dissolved in the metal during heating and the C precipitates into its crystalline form on cooling at C/metal interface. In this work, multilayer *a*-C/Co composites are fabricated using rapid thermal annealing (RTA) and the structures and magnetic properties of those composites are

* Corresponding author.
** Corresponding author.
*** Corresponding author.
E-mail addresses: hshsu@mail.nptu.edu.tw (H.-S. Hsu), chin.yiying@nsrrc.org.tw (Y.-Y. Chin), sjs@nuk.edu.tw (S.-J. Sun).

http://dx.doi.org/10.1016/j.carbon.2016.12.060
0008-6223/

investigated. Magnetization reveals an EB at the interface between Co and graphitic C in the *a*-C matrix after RTA via AFM/FM coupling. This is further supported by XMCD measurements and theoretical calculations. The present work makes an advance in this field, because it reports an EB effect in a C based material.

2. Experimental

Discontinuous [*a*-C(d)/Co(3 nm)]$_5$/C(3 nm) multilayers with d = 3 nm and d = 6 nm were fabricated on a quartz substrate at ambient temperature using a radio frequency sputtering system with a base pressure of ~2 × 10^{-6} Torr. Several Co/C multilayers were deposited using sputtering with Ar gas at a process pressure of ~2 × 10^{-2} Torr alternately on C and Co targets for five cycles. Radio frequency sources were used to generate the plasma. The substrate wafers on which the films were deposited are fixed in holders on a rotating platen in a sputter-up configuration. The Co/C multilayers were deposited alternately on C and Co targets for five cycles. The sputter gun to turn on or off for certain desired thicknesses controlled by use of quartz crystal monitoring. After deposition, RTA was performed at 600 °C for 2 min in a vacuum chamber that was evacuated to ~8 × 10^{-6} Torr. Magnetization measurements were made using a super-conducting quantum interference device (SQUID) (MPMS, Quantum Design Co., Ltd.). The field cooling (FC) hysteresis loops were measured at 10 K under cooling fields of 1T. XAS measurements were made in the wiggler-C beam line 17 (at the Taiwan Light Source in Hsinchu, Taiwan) and a fluorescent yield spectrum was obtained to determine the bulk properties of the films. XMCD measurements were performed at the Dragon beam line BL11A of Taiwan Light Source. XMCD spectra were measured by the TEY method and the circular polarization of the incident photons was fixed and the direction of the applied magnetic field was changed. HRTEM measurements were performed on a JEOL-JEM2100F instrument operating at an acceleration voltage of 200 kV.

3. Results and discussion

3.1. The observation of EB in C/Co after RTA

Fig. 1 shows the magnetic field dependent magnetization (M-H) data with the applied field along the in-plane axis for (a) d = 3 nm and (b) d = 6 nm *a*-C/Co composites with and without RTA at 10 K. The coercivities of as deposited C/Co multilayers are much larger than those of as-deposited Co films without C. It implies the presence of Co_3C or Co_2C. Co_3C or Co_2C structures can provide an enhancement to the coercivity (see in Fig. S1 in the supplementary data). The decomposition of the metastable Co_3C and Co_2C carbides proceeds at temperatures of 250 °C and 520 °C, respectively [29–31]. Therefore, an annealing temperature of 600 °C was chosen to decompose the metastable C–Co bonds and form adequate C/Co interfaces. In contrast to the nearly symmetric M-H data of the as grown samples, the hysteresis loops of these samples after RTA significant shifted to the left of the zero field axis, clearly indicating pronounced EB. The EB fields for d = 3 nm and d = 6 nm samples after RTA (given by the shift of the hysteresis loop along the H-axis) are H_E 503 Oe and 291 Oe, respectively. The $T^{1/2}$ dependence of Hc(T) (shown in Fig. 1(c)) is a signature of thermal fluctuations dominating domain wall motion energetics and exchange coupling [32]. The blocking temperature, T_B, (i.e., the temperature at which biasing vanishes) for these samples is about 200 K as shown in Fig. 1(d). It is noted that a small EB also exists in the as-grown sample. The observation of EB in our as grown samples might imply the presence of antiferromagnetic CoO in the neighborhood of ferromagnetic material. Therefore, CoO is likely to play some role in our observed significant EB for our RTA samples. However, the magnitude and the T_B are much smaller than those of RTA samples (see Fig. S2(a) in the supplementary data). On the other hand, the significant EB can also be observed in the zero field cooling (ZFC) M-H loop at 10 K for the d = 3 RTA sample but is absent for the as grown sample, as displayed in Fig. S2(b). However, in general, the EB effect in Co/CoO system is induced by FC [33–35]. In addition, Co films after high vacuum RTA without C do not exhibit apparent EB after FC (see Fig. S1 in the supplementary data) even at 10 K. Therefore, it implies the magnetic interaction between Co and C should play the main role for the observed EB in RTA samples. But this kind of magnetic interaction cannot persist above 200 K even though Curie temperature of Co is much higher. Therefore, the EB effect is seen to vanish at about 200 K in both d = 3 and d = 6 RTA samples. Further electronic- and micro-structures studies are necessary to clarify the phenomenological characteristics of this EB effect in *a*-C/C films after RTA.

3.2. Local structures, electronic structures, and microstructures of *a*-C/Co with and without RTA

Extended x-ray absorption fine structure (EXAFS) spectroscopy, a specialized version of X-ray absorption spectroscopy (XAS), was used to show the local structures that surrounded the Co atoms [36]. Fig. 2(a) plots the radial distribution function, the Fourier-transformed (FT) EXAFS amplitude of extended x-ray absorption fine structure (EXAFS), on the Co *K*-edge for these samples; it also plots the function on the Co-*K* edge of Co metal as a reference. In addition to the peak associated with Co–Co bonding near 2.2 Å, the spectra of the as-grown *a*-C/Co sample also includes the peaks around 1.7 Å, probably associated with C–Co bonding [31,37]. It changes significantly after RTA. The Co *K*-edge FT spectra are very similar to spectra from Co metal. The results demonstrate that, in RTA, most of the C–Co bonding decomposes and Co atoms form metallic states. This point is important when considering magnetic effects in our theoretical model. On the other hand, X-ray absorption near-edge structure (XANES) spectroscopy is a powerful tool for identifying the electronic states, and particularly the valence states of TM elements, it was applied here. Fig. 2(b) presents the XANES spectra on the Co *K*-edge of the d = 3 nm and d = 6 nm samples with and without RTA, together with that of a standard Co metal for comparison. Unlike the clear shoulder around 7712 eV in the Co metal spectra, the pre-edge features for d = 3 nm and d = 6 nm samples without RTA, which can be related to the transition to bound states. In addition, both samples include a comparatively strong white line, which indicates a high unoccupied states concentration. We conclude that in these samples, electrons transfer process from Co atoms onto C neighbors is responsible for the empty states of Co. Therefore, we suppose that the enhancement of XANES white line is induced by the appearance of metastable bonding [31]. After RTA, the carbide is decomposed, and therefore most of the Co atoms in d = 3 nm and d = 6 nm samples are close to the +0 metallic state. These results are consistent with our EXAFS data. However, it is noted that the difference near the white line of the XANES data between Co metal and RTA samples implies the empty density of states (DOSs) of Co result from the hybridization between Co atoms and graphitic like neighbors at the C/Co interfaces. Because graphitic like neighbors contain a large number of unpaired electrons on the surfaces. It is possible to expect the hybridization between C and Co atoms. The d = 3 nm sample after RTA yields a spectrum that is between that of the d = 6 nm sample after RTA and that of metallic Co. It indicates the d = 6 nm sample after RTA reveals more unoccupied DOSs than the d = 3 nm sample, implying a stronger hybridization due to more electrons transfer from Co to C. A combination of EXAFS and XANES

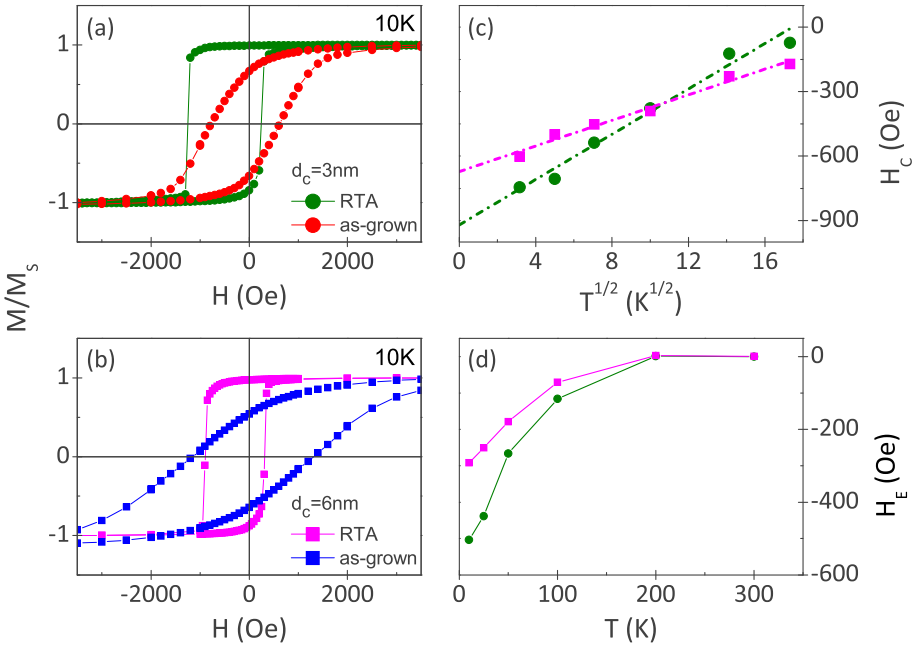

Fig. 1. The M-H data for (a) d = 3 nm and (b) d = 6 nm Co:*a*-C composites without and with RTA at 10 K. (c) The $T^{1/2}$ dependence of Hc(T) of d = 3 nm and d = 6 nm samples after RTA, with the dash line being a guide to the eye. (d) Temperature dependence of the exchange bias field, H_E, of the d = 3 nm and d = 6 nm samples after RTA. (A colour version of this figure can be viewed online.)

data reveals that most of the Co elements form metallic Co and these phases tend to be surrounded by graphitic neighbors with quasi-sp^2 orbital configurations after RTA.

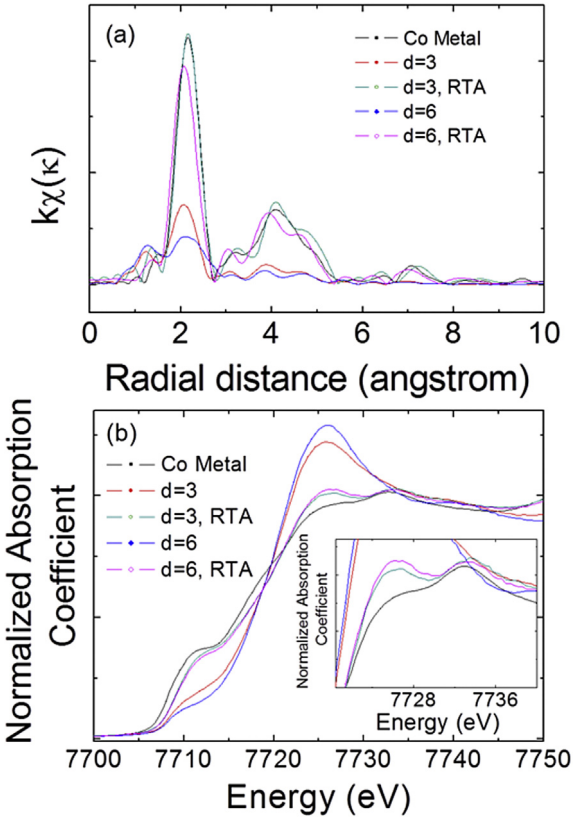

Fig. 2. (a) The FT amplitude of EXAFS of d = 3 nm and d = 6 nm Co:*a*-C composites without and with RTA as well as metallic Co foil. (b) XANES for these samples at Co *K*-edge. Metallic Co foil data is provided for reference. (A colour version of this figure can be viewed online.)

High resolution transmission electron microscopy (HRTEM) measurements provide further information regarding microstructures. Fig. 3 shows the HRTEM cross section images of the d = 3 nm sample with and without RTA. For the as-grown sample (Fig. 3 inset), a multilayered structure with a periodic parallel dark lines from "quasi 2D" Co layers, separated by C nominal layers, was observed. The *a*-C region shows a gray "gravel-like" appearance that can be modeled as a random network. Some of the Co diffused

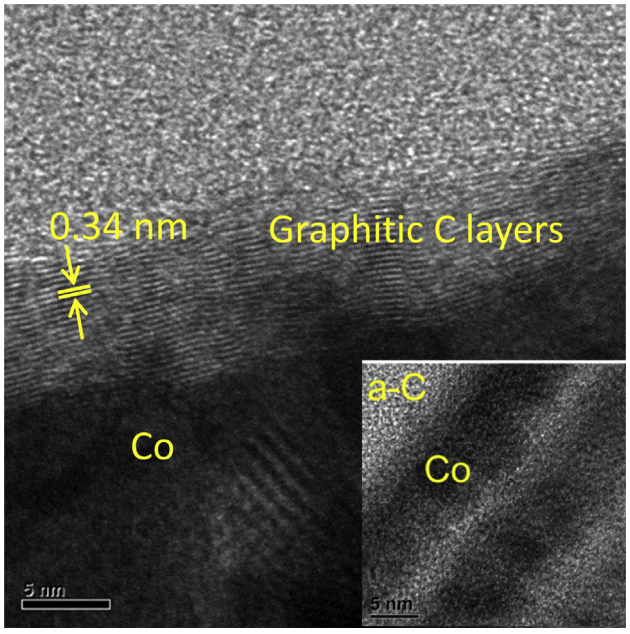

Fig. 3. The HRTEM image of the d = 3 nm Co:*a*-C composites with RTA. The graphitic layers region showing a characteristic 0.34 nm interplanar spacing. The inset shows the HRTEM image without RTA for underscoring how essential the annealing is in the metal-contact-induced graphitization mechanism. (A colour version of this figure can be viewed online.)

outward during the sputtering process. Therefore, the average spacing between Co layers is less than 3 nm. Our EXAFS and XANES results suggest that some Co atoms mixed with C and formed C—Co bonding near C/Co interfaces. In contrast, for *a*-C/Co after RTA, some of the Co diffused outward and formed Co clusters that contacted each other, as revealed in Fig. 3. In addition, another significant feature is that which lies at the C/Co layer. The C microstructure there has gained a less random configuration, which consists of small graphene multilayers. The dark lines at the *a*-C - Co interface are consistent with a material that has partially crystallized [24,25]. The measured layer separation is about 0.34 nm, which is close to the (002) interplanar spacing of the bulk graphite layers. The d = 6 nm samples with and without RTA show similar microstructural transformation to those found in d = 3 nm samples.

3.3. Magnetic coupling in C/Co composites

The existence of a considerable magnetic interaction between the C and the Co could be revealed by XMCD applied to the Co-$L_{2,3}$ and C-*K* because XMCD is element and site selective. Before discussing the XMCD data, we would like to look into the spectral features at the Co-$L_{2,3}$ edges first. Fig. 4(a) presents the X-ray absorption spectra of the C/Co composites at 25 K recorded in the total electron yield mode together with that of CoO single crystal measured simultaneously. The energy position of the C/Co composites is very close to that of CoO, indicating the same valence state of Co in C/Co composites. Moreover, one could observe the multiplet structures of all the measured samples and the spectral structures of the as-grown C/Co composites are rather similar to those of CoO, implying the partial oxidization of Co in those samples on the surfaces. The presence of CoO is responsible to the weak EB in as-grown samples, as discussed above. However, the broader main peak of the C/Co composites after RTA might result from the higher content of metallic Co or the hybridization between C and Co, as suggested by the EXAFS and Co-*K* XANES results. Because the significant EB cannot be observed in RTA Co films without C, the C should play an important role for the observed phenomena. To obtain more information concerning the electronic structures of C, the C-*K* XAS experiments were performed. The C-*K* XAS spectra of those C/Co composites are presented in Fig. 4(b). Spectra features in this region were expected to correspond to the C $1s \rightarrow \pi^*$ transition [17,38,39]. Compared with the as-grown C/Co composites, those samples after RTA possess one significant low-energy feature at around 285 eV, which can be linked to the excitation from C 1s level to empty π^*-states associated to the sp^2 bonded C atoms. It is consistent with our TEM data that graphitization can occur after RTA. Furthermore, this structure in the d = 3 nm RTA sample is more obvious than that in the d = 6 nm RTA sample, implying more empty π^*-states exist in the d = 3 nm RTA sample. It is also consistent with the Co XANES that the d = 6 nm RTA sample reveals a stronger hybridization signal. Because RTA includes a diffusional process, the metal phase also acts as a nucleation site for the C. To understand the magnetic interactions as well as the influence of the RTA, we performed XMCD experiments on the C/Co composites.

The left panel of Fig. 4(c) shows normalized total electron yield (TEY) XMCD spectra for Co-$L_{2,3}$ edges at 25 K from the d = 3 nm with and without RTA, with a magnetic field of 1 T applied as it cooled from 300 K. 25 K is the lowest temperature our XMCD setup could reach. The size of the beam spot is around 2 × 1 mm^2, which is much larger than the domain size. Therefore, the XMCD signal is averaged-out over the domains. Co XMCD around 779eV and 795 eV corresponds to the L_3 and L_2 magnetically coupled spin transitions, respectively. The XMCD curves of the C/Co composites are quite different from that of Co^{2+} in $LaMn_{0.5}Co_{0.5}O_3$, indicating distinct magnetic contribution [40]. For C/Co composites, the XMCD

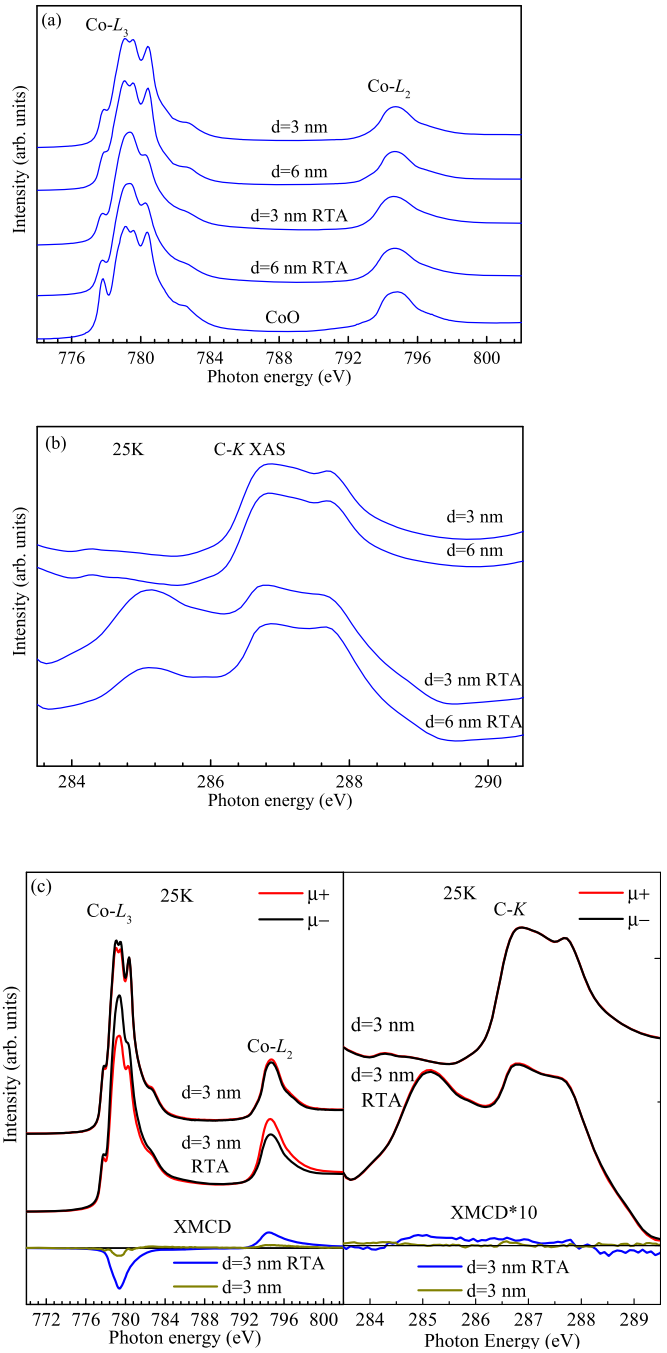

Fig. 4. XMCD spectra of the d = 3 nm and d = 6 nm Co:*a*-C composites with RTA: absorption spectra measured for two opposite orientations of the magnetization are shown in the upper part for the Co $L_{2,3}$- (a) and C *K*-edges (b). The corresponding differences are shown in the lower part of the respective Figures. (A colour version of this figure can be viewed online.)

curves are much broad and multiplet structures are hardly to be observed. The broad XMCD is similar to that of the Co metal [41,42], implying that metallic Co contributes mainly to the magnetic interactions in all the measured samples, as what was found in the Co-doped TiO_2 [43]. Moreover, similar to what observed in the Co-doped TiO_2 study, the RTA induces more metallic Co and thus much stronger XMCD accompanying the broader XAS features. Although the XAS spectra of the C/Co composites exhibit multiplet structures, their ferromagnetic properties are mainly contributed by the metallic Co, like the case of the Co-doped TiO_2 [43]. To obtain

further information concerning the magnetic interactions in these samples, the XMCD sum rules were applied to extract the orbital and spin moments of Co in the C/Co composite with d = 3 nm after RTA [41,44,45]. The orbital and spin moments of d = 3 nm after RTA are 0.076 and 0.80, respectively. On the other hand, the as-grown C/Co composites possess rather weak XMCD signal, indicating less magnetic moments in those samples. Moreover, the ratio of orbital to spin moment of d = 3 nm after RTA is remarkably close to that of pure Co films [41].

As presented in the right panel of Fig. 4(c), a small but vivid C-*K* XMCD signal could be observed from approximately 286 to 288 eV for d = 3 nm after RTA, and is antiparallel to the XMCD signal at the Co-$L_{2,3}$. Therefore, the finite XMCD signal indicates the presence of the induced magnetic moment of C atoms in the C/Co composites after RTA. The extra feature at 285 eV of the sample after RTA also exhibits XMCD signal, which may have originated from the strong hybridization between C π^* and transition metal 3*d* valence band states near graphitic C/Co interfaces. The C XMCD is antiparallel to that of Co, giving the hint about the origin of the Co/C EB effect as discussed below.

Furthermore, as predicted by the theoretical studies on the branching ratio (I(L_3)/[I(L_3) + I(L_2)]; BR), one can detect the spin-orbit coupling as well as the localization of the 3*d* electrons by XAS [46–48]. Recent experimental studies observed the influence of hybridization and localization on the BR [49–52]. Hence, we had managed to subtract the backgrounds of the Co-$L_{2,3}$ spectra to obtain the BRs of those samples. We found that the large BR of the C/Co composites (0.778–0.798) is close to the value of the small Co clusters [50] and much higher than the value of bulk Co (0.66) and Co_2MnSi thin films [49,50], indicating the presence of the hybridization between Co and C. This is consistent with our XANES results regarding the Co K edge. We have also measured XMCD of those samples at room temperature. In contrast to slightly weaker Co XMCD signal, the C XMCD signal is much weaker and close to our detection limit (see in Fig. S3 in the supplementary data). It further indicates the presence of EB can be concluded from the appearance of C XMCD signal.

3.4. Theoretical modeling of the magnetic interfaces in graphitic C/Co

By a combination of XAS, HRTEM, and element specific XMCD data, the EB effect can be related to the interactions at the graphitic C/Co interface. The presence of an antiferromagnetic exchange coupling of the interfacial layers of TM and C with weakly induced magnetism caused by a magnetic proximity effect has been reported [17,18]. However, the EB effect in graphitic C/TM has not been observed in these cases. The magnetic moments induced on our graphitic C in an *a*-C matrix are more localized than those on the graphene surface with ordered sp^2 hybridization due to the structure disordered. Therefore, the localized C magnetic moments could pin the Co moments and result in a sizeable EB effect. The carbides are formed in as grown samples near Co/C interfaces. Therefore, we cannot observe significant EB in our as grown samples.

As has been mentioned, EB will happen when the system has coupling interfaces between AFM and FM materials and the critical temperature of the former is lower than that of the latter. Our experimental results clearly show the EB phenomena as the samples are treated with annealing processes. Results explicitly imply that the graphite style carbon of interfaces (GCI) enter AFM states after thermal annealing.

Based on the experimental results we construct a theoretical model to calculate the magnetization of Co nanoparticles in the interfaces as a function of particular magnetic couplings. The magnitude of the EB effect is dominated by the spin alignments and can be clarified by the measurement of spin moments. The following theoretical model will take into account the spin moments in the interfaces of Co and C atoms. The essential magnetic interaction in GCI is paramagnetic and it will be transformed to be AFM. We supposed that the magnetic transformations arise from the Co atoms introducing strong Coulomb interactions to GCI as the Co atoms approach the C atoms through thermal driving. From the Hubbard model simulations the ground state of a system with strong Coulomb interactions tends to be AFM and the increased Coulomb interactions can be promoted from both effects of the quantum confinement and the Coulomb screening reduction in the Co nanoparticles. Because the structure is disordered which causes the conduction carriers of GCI to achieve a certain degree of localization. Even the conduction carriers of GCI are localized but still possess a certain degrees of freedom in conduction because GCI possesses dominant sp^2 orbits. Thus, as the Co atoms approach the GCI, a strong AFM coupling is formed between Co nanoparticles and the GCI by means of Kondo interactions. Namely, the Co nanoparticles antiferromagnetically interact with GCI and the magnetic interactions between the localized conduction carriers of GCI are AFM as well; furthermore, because the carriers are localized, their hopping integrals are less than that of graphene. Essentially, the magnetization of Co is induced from the RKKY interaction via second order Kondo interactions [53,54], where the conduction carriers of GCI are the medium.

The Hamiltonian of the model is,

$$\mathrm{H} = \mathrm{H}_0 + H_K + H_J, \tag{1}$$

H_0 is the conduction band of graphited carbon. For simplicity we set the structure of graphited carbon to a graphene structure. The formula of H_0 is,

$$\mathrm{H}_0 = \sum_{k,\sigma} \varepsilon_k c^+_{k,\sigma} c_{k,\sigma}. \tag{2}$$

ε_k is the band dispersion of the conduction band of GCI in the momentum *k* representation; σ is the spin index of the conduction carriers; their creation and annihilation operators are c^+ and c, respectively. The band dispersion ε_k is derived from the hopping integral t and the structure dispersion factor of graphene $\gamma_\mathrm{k} = \left(1 + 4\cos\left(\frac{\sqrt{3}k_x}{2}a\right)\cos\left(\frac{k_y}{2}a\right) + 4\cos\left(\frac{k_y}{2}a\right)^2\right)^{\frac{1}{2}}$ with the lattice constant *a*, and which can be written as $\varepsilon_\mathrm{k} = \pm t\,\gamma_k$.

H_K, which represents the Kondo interactions between the local magnetic moments of Co nanoparticles and the conduction carriers of GCI, is written as,

$$\mathrm{H}_\mathrm{k} = J_k c \sum_i S_i \cdot \sigma_i, \tag{3}$$

where J_k is the antiferromagnetic Kondo coupling between the magnetic moment of Co nanoparticles, S_i, and the spins, σ, of conduction carriers of GCI. The constant c represents the density of magnetic local moment on each carbon site, and *i* is the site index.

H_J, induced from the Coulomb interactions by Co nanoparticles, represents the AFM interactions between the spins of conduction carriers of GCI, and can be written as,

$$\mathrm{H}_\mathrm{J} = \mathrm{J} \sum_{ij} \sigma_i \cdot \sigma_j, \tag{4}$$

where J is the antiferromagnetic coupling and σ_i represents the spin of conduction carriers in carbon site *i*. All Co ions with spin S_i in our

model are located in the GCI.

To calculate the expectation value of magnetic moments of local spins of Co nanoparticles, m ($<S_z>$), Green's function theory was employed, and the magnon dispersion could be calculated. The magnon excitation can be written in a form that encapsulates Eqs. (6) and (7),

$$\omega(q) = -cJ_k <\sigma_z> + \frac{1}{2}c^2 J_k \sum_p \frac{(6)}{(7)}. \quad (5)$$

$\omega(q)$, is the magnon dispersion as a function of magnon momentum q, which can be solved self-consistently because Eq. (7) is also a function of $\omega(q)$; where Eqs. (6) and (7) in Eq. (5) are,

$$<c^+_{p+q,\uparrow} c_{p+q,\uparrow}> - <c^+_{p,\downarrow} c_{p,\downarrow}> \quad (6)$$

and

$$\omega(q) - \varepsilon_{p,\downarrow} + \varepsilon_{p+q,\uparrow} + 6J<\sigma_z> - J\gamma_q \sum_{p'} \Big(<c^+_{p'+q,\uparrow} c_{p'+q,\uparrow}> - <c^+_{p',\downarrow} c_{p',\downarrow}> \Big); \quad (7)$$

$<\sigma_z>$ is the expectation value of magnetic moment of conduction carriers of graphited carbon; γ_q is the structure dispersion factor; the spin dependent band dispersion can be written in the form, $\varepsilon_{p,\sigma} = \varepsilon_p + \sigma J_k m$.

As the magnon dispersion is obtained in terms of the expectation value of the magnetic moment of Co nanoparticles, m can be calculated in terms of Callen's formula,

$$m = \frac{[S - \Phi(S)][1 + \Phi(S)]^{2S+1} + [S + 1 + \Phi(S)][\Phi(S)]^{2S+1}}{[1 + \Phi(S)]^{2S+1} - [\Phi(S)]^{2S+1}}, \quad (8)$$

$\Phi(S)$ is called the magnon number function and it can be written as $\Phi(S) = \sum_q \frac{1}{\exp(\beta\omega(q))-1)}$ and β is the inverse of temperature energy, $\beta = 1/K_b T$.

In our model the J is less than J_k because Co is a strong ferromagnetic material and the antiferromagnetic coupling J is a second order parameter. For this reason even though the conduction carriers of GCI are antiferromagnetic, when they interact, there still exists a small value of ferromagnetization $<\sigma_z>$.

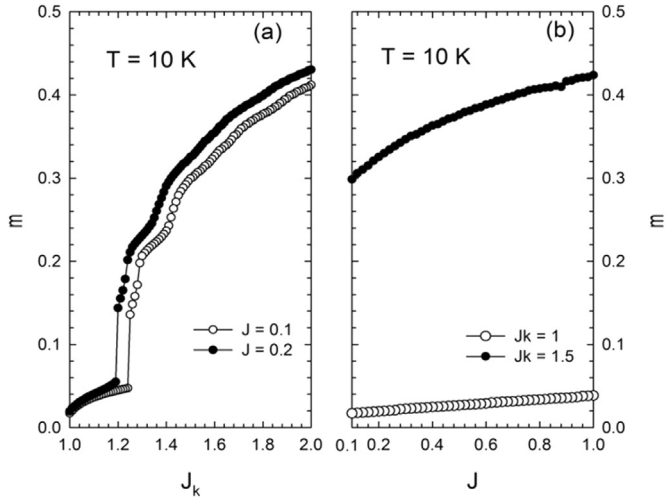

Fig. 5. The expectation value of magnetic local moment m in Co nanoparticles at temperature 10 K. (a) The magnetic moment m as a function of J_k for J = 0.1 and J = 0.2, respectively. (b) The magnetic moment m as a function of J for J_k = 1 and J_k = 1.5, respectively. The unit of couplings scaled by hopping integral of conduction band is set to 1 and the c value in Eq. (3) is set to 0.1 as well.

Our theoretical results in Fig. 5(a) show that the Kondo interaction increases the Co magnetization, which is consistent with the experimental results as shown in Fig. 1, where the magnetization of samples at zero magnetic field increases after thermal annealing because thermal annealing enhances the Kondo interaction. An obvious transition in each curve of Fig. 5 (a) arises from a competition between both AFM interactions, namely: the Kondo interaction between Co nanoparticles and GCI, and the AFM interactions between conduction carriers of GCI. Both competing interactions and different spin alignments will cause spin frustrations, as J_k increases a threshold is reached and the magnetic frustration on GCI is suppressed. Essentially, the transition happens at the same time as the suppression of the magnetic frustrations. Interestingly, the increase of J will enhance the magnetization of Co, as shown in Fig. 5(b). The enhancement of magnetization with the increase of J is due to the increase of spin frustration which also causes spin fluctuations on GCI and tends to promote the RKKY interaction. Eventually, as this transformation proceeds, J_k and J are the dominant and secondary factors for forming Co magnetization. According to our model, the observation of larger EB field of d = 3 nm with RTA than that of d = 6 nm, as displayed in Fig. 1(d), can be understood. By our C XAS measurements the d = 3 nm RTA sample reveal more disordered sp^2 states would have more carrier localization and result in a larger Kondo coupling. Besides, based on Co XANES the hybridization due to charge transfer between Co and GCI in the d = 6 nm RTA sample is larger than in the d = 3 nm RTA sample, which is consistent with the prediction from our theoretical model. Because the hybridization will suppress the carrier localization and Kondo effect as well as the appearance of EB.

4. Conclusion

In summary, an EB effect can be observed in graphitic C/Co composites synthesized through RTA on Co/*a*-C multilayers. The appearance of EB effect reveals an antiparallel alignment between the sp^2-bonded C and the metallic Co in the composites. The C/Co hybridization is evidenced by the induced C moment by XMCD measurements. The weaker electrons' hybridizations of the d = 3 nm sample after RTA than that of d = 6 nm sample after RTA can be explained by the increase of the AFM interactions in the GCI and the Kondo interactions in the interfaces between the GCI and Co according to our theoretical model. The present study provides a deeper understanding of EB in graphitic C/Co composites, which may be important for guiding the design and fabrication of C based spintronics devices.

Acknowledgements

The authors would like to thank the Ministry of Science and Technology of the Republic of China, Taiwan, for financially supporting this research under Contract No. MOST 104-2112-M-153 -002 -MY3 (Hua-Shu Hsu), MOST 103-2112-M-213-004-MY3 (Hong-Ji Lin), and MOST 104-2112-M-390-001 (Shih-Jye Sun). We are thankful also to the President of Russia Program of support the leading scientific schools, grant NSh-7559,2016.2 (SGO).

Appendix A. Supplementary data

Supplementary data related to this article can be found at http://dx.doi.org/10.1016/j.carbon.2016.12.060.

References

[1] J. Nogués, I.K. Schuller, Exchange bias, J. Magn. Magn. Mater. 192 (1999) 203–232.
[2] A.E. Berkowitz, K. Takano, Exchange anisotropy-a review, J. Magn. Magn. Mater. 200 (1999) 552–570.
[3] F. Radu, H. Zabel, Exchange bias effect of ferro-/antiferromagnetic heterostructures, Springer Tr. Mod. Phys. 227 (2008) 97–184.
[4] C. Binasch, P. Grünberg, F. Saurenbach, W. Zinn, Enhanced magnetoresistance in layered magnetic structures with antiferromagnetic interlayer exchange, Phys. Rev. B 39 (1989) 4828–4830.
[5] F. Radu, R. Abrudan, I. Radu, D. Schmitz, H. Zabel, Perpendicular exchange bias in ferromagnetic spin valves, Nat. Commun. 3 (2012), 715/1–7.
[6] P. Tian, X. Zhang, Q.Z. Xue, Enhanced room-temperature positive magnetoresistance of a-C: Fe films, Carbon 45 (9) (2007) 1764–1768.
[7] X. Zhang, C. Wan, L. Wu, A bias voltage dependent positive magnetoresistance in Co_x–C_{1-x}/Si heterostructure, Appl. Phys. Lett. 95 (2) (2009), 022503/1–3.
[8] Y.C. Jiang, J. Gao, Positive colossal magnetoresistance observed in Co doped amorphous carbon/silicon heterostructures, Appl. Phys. Lett. 101 (18) (2012), 182401/1–3.
[9] H.S. Hsu, P.Y. Chung, J.H. Zhang, S.J. Sun, H. Chou, H.C. Su, et al., Observation of bias-dependent low field positive magneto-resistance in Co-doped amorphous carbon films, Appl. Phys. Lett. 97 (3) (2010), 032503/1–3.
[10] Z.W. Fan, P. Li, E.Y. Jiang, H.L. Bai, High spin polarization induced by the interface hybridization in Co/C composite films, Carbon 50 (12) (2012) 4470–4475.
[11] E. Cobas, A.L. Friedman, O.M.J. van't Erve, J.T. Robinson, B.T. Jonker, Graphene as a tunnel barrier: graphene-based magnetic tunnel junctions, Nano Lett. 12 (2012) 3000–3004.
[12] A.L. Friedman, H. Chun, Y.J. Jung, D. Heiman, E.R. Glaser, L. Menon, Possible room-temperature ferromagnetism in hydrogenated carbon nanotubes, Phys. Rev. B 81 (2010), 115461/1–4.
[13] A.L. Friedman, O.M.J. van 't Erve, C.H. Li, J.T. Robinson, B.T. Jonker, Homoepitaxial tunnel barriers with functionalized graphene-on-graphene for charge and spin transport, Nat. Commun. 5 (2014), 3161/1–6.
[14] A.L. Friedman, O.M.J. van 't Erve, J.T. Robinson, K.E. Whitener Jr., B.T. Jonker, Hydrogenated graphene as a homoepitaxial tunnel barrier for spin and charge transport in graphene, ACS Nano 9 (2015) 6747–6755.
[15] V.M. Karpan, P.A. Khomyakov, A.A. Starikov, G. Giovannetti, M. Zwierzycki, M. Talanana, et al., Theoretical prediction of perfect spin filtering at interfaces between close-packed surfaces of Ni or Co and graphite or graphene, Phys. Rev. B 78 (2008), 195419/1–11.
[16] P. Dev, T.L. Reinecke, Substrate effects: disappearance of adsorbate-induced magnetism in graphene, Phys. Rev. B 89 (2014), 035404/1-5.
[17] Dedkov YuS, M. Fonin, Electronic and magnetic properties of the graphene–ferromagnet interface, New J. Phys. 12 (2010), 125004/1–22.
[18] W.Q. Liu, W.Y. Wang, J.J. Wang, F.Q. Wang, C. Lu, F. Jin, et al., Atomic-scale interfacial magnetism in Fe/Graphene heterojunction, Sci. Rep. 5 (2015), 11911/1–9.
[19] T. Moorsom, M. Wheeler, T. Mohd Khan, F. Al Ma'Mari, C. Kinane, S. Langridge, et al., Spin-polarized electron transfer in ferromagnet/C_{60} interfaces, Phys. Rev. B 90 (2014), 125311/1–6.
[20] H.S. Hsu, P.C. Chien, S.J. Sun, Y.Y. Chang, C.H. Lee, Room temperature ferromagnetism in Co-doped amorphous carbon composites from the spin polarized semiconductor band, Appl. Phys. Lett. (2014) 105, 042410/1-4.
[21] H.S. Hsu, P.E. Lu, C.W. Chang, S.J. Sun, C.H. Lee, H.C. Su, et al., Tunable interface magnetic-optical properties of Co doped amorphous carbon film induced by charge transfer after acid treatment, Carbon 77 (2014) 398–404.
[22] P.K. Manna, S.M. Yusuf, Two interface effect: exchange bias and magnetic proximity, Phys. Rep. 535 (2014) 61–99.
[23] J. Robertson, Diamond like amorphous carbon, Mater Sci. Eng. R37 (2002) 129–281.
[24] T. Hayashi, S. Hirono, M. Tomita, S. Umemura, Magnetic thin film of cobalt nanocrystals encapsulated in graphite-like carbon, Nature 381 (1996) 772–774.
[25] A.G. Ramírez, T. Itoh, R. Sinclair, Crystallization of amorphous carbon thin film in the presence of magnetic media, J. Appl. Phys. 85 (1999) 1508–1513.
[26] J.J. Host, J.A. Block, K. Parvin, V.P. Dravid, J.L. Alpers, T. Sezen, et al., Effect of annealing on the structure and magnetic properties of graphite encapsulated nickel and cobalt nanocrystals, J. Appl. Phys. 83 (2) (1998) 793–801.
[27] M. Zheng, K. Takei, B. Hsia, H. Fang, X.B. Zhang, N. Ferralis, et al., Metal-catalyzed crystallization of amorphous carbon to graphene, Appl. Phys. Lett. 96 (2010), 063110/1–3.
[28] A.H. Lu, W.C. Li, N. Matoussevitch, B. Spliethoff, H. Bönnemann, F. Schü th, Highly stable carbon-protected cobalt nanoparticles and graphite shells, Chem. Commun. 1 (2005) 98–100.
[29] R.S. Iskhakov, S.V. Stolyar, L.A. Chekanova, E.M. Artem'ev, V.S. Zhigalov, High pressure phases in nanocrystalline Co(C) films obtained by pulsed plasma vaporization, JETP Lett. 72 (2000) 316–319.
[30] V.G. Harris, Y. Chen, A. Yang, S. Yoon, Z. Chen, A.L. Geiler, et al., High coercivity cobalt carbide nanoparticles processed via polyol reaction: a new permanent magnet material, J. Phys. D. Appl. Phys. 43 (2010), 165003/1–7.
[31] H.S. Hsu, W.Y. Su, P.C. Chien, S.T. Kuo, S.J. Sun, P.Y. Chuang, et al., Sizeable magnetic circular dichroism of artificially precipitated Co clusters in amorphous carbon, AIP Adv. (2012) 2, 032142/1-6.
[32] H.C. Su, M.J. Huang, H.J. Lin, C.H. Lee, C.T. Chen, C.H. Liu, et al., Connection between orbital moment enhancement and exchange bias in a $[Ni_{80}Fe_{20}/Mn]_3$ multilayer, Phys. Rev. B (2013) 87, 014402/1-6.
[33] D.L. Peng, K. Sumiyama, T. Hihara, S. Yamamuro, T.J. Konno, Magnetic properties of monodispersed Co/CoO clusters, Phys. Rev. B 261 (2000) 3103–3109.
[34] I.S. Zhidkov, N.A. Skorikov, A.V. Korolev, A.I. Kukharenko, E.Z. Kurmaev, V.E. Fedorov, S.O. Cholakh, et al., Electronic structure and magnetic properties of graphene/Co composites, Carbon 91 (2015) 298–303.
[35] D. Nissen, O. Klein, P. Matthes, M. Albrecht, Exchange-biased Py/CoO vortex structures: magnetization reversal, cooling-field dependence, and training, Phys. Rev. B 94 (2016), 134422/1–6.
[36] G. Bunker, Introduction to XAFS: a Practical Guide to X-ray Absorption Fine Structure Spectroscopy, Cambridge Univ Press, 2010.
[37] A.V. Kolobov, J. Tominaga, T.K. Zvonareva, V.I.I. Omskii, H. Oyanagi, Local structure of Co nanocrystals embedded in hydrogenated amorphous carbon: an x-ray absorption study, J. Appl. Phys. 92 (10) (2002) 6195–6199.
[38] N. Jaouen, D. Babonneau, J.M. Tonnerre, D. Carbone, F. Wilhelm, A. Rogalev, et al., Spin and orbital magnetic moments in carbon-encapsulated $Fe_{50}Pt_{50}$ nanoparticles, Phys. Rev. B 76 (2007), 104421/1–5.
[39] Y. Muramatsu, K. Shimomura, T. Katayama, E.M. Gullikson, Total electron yield soft X-ray absorption spectroscopy in the C *K* region of the mixtures of graphitic carbons and diamond for quantitative analysis of the sp^2/sp^3-hybridized carbon ratio, Jpn. J. Appl. Phys. (2009) 48, 066514/1-4.
[40] T. Burnus, Z. Hu, H.H. Hsieh, V.L.J. Joly, P.A. Joy, M.W. Haverkort, H. Wu, et al., Local electronic structure and magnetic properties of $LaMn_{0.5}Co_{0.5}O3$ studied by x-ray absorption and magnetic circular dichroism spectroscopy, Phys. Rev. B 77 (2008), 125124/1–7.
[41] C.T. Chen, Y.U. Idzerda, H.J. Lin, N.V. Smith, G. Meigs, E. Chaban, et al., Experimental confirmation of the XMCD sum rules for iron and cobalt, Phys. Rev. Lett. 75 (1995) 152–155.
[42] C. Ge, X. Wan, E. Pellegrin, Z. Hu, S.M. Valvidares, A. Barla, et al., Direct observation of rotatable uncompensated spins in the exchange bias system Co/CoO–MgO, Naoscale 5 (2013) 10236–10241.
[43] J.Y. Kim, J.H. Park, B.G. Park, H.J. Noh, S.J. Oh, J.S. Yang, et al., Ferromagnetism induced by clustered Co in Co-doped anatase TiO_2 thin films, Phys. Rev. Lett. (2003) 90, 017401/1-4.
[44] B.T. Thole, P. Carra, F. Sette, G. van der Laan, X-ray circular dichroism as a probe of orbital magnetization, Phys. Rev. Lett. 68 (1992) 1943–1946.
[45] P. Carra, B.T. Thole, M. Altarelli, X. Wang, X-ray circular dichroism and local magnetic fields, Phys. Rev. Lett. 70 (1993) 694–697.
[46] B.T. Thole, G. van der Laan, Branching ratio in x-ray absorption spectroscopy, Phys. Rev. B 38 (1988) 3158–3171.
[47] B.T. Thole, G. van der Laan, Linear relation between x-ray absorption branching ratio and valence-band spin-orbit expectation value, Phys. Rev. A 38 (1998) 1943–1947.
[48] G. van der Laan, B.T. Thole, Local probe for spin-orbit interaction, Phys. Rev. Lett. 60 (1988) 1977–1980.
[49] E. Arenholz, N. Telling, P. Keatley, L. Shelford, E. Arenholz, G. van der Laan, et al., Temperature dependence of the interface moments in Co_2MnSi thin films, Appl. Phys. Lett. 92 (2008), 192503/1–3.
[50] J.T. Lau, J. Rittmann, V. Zamudio-Bayer, M. Vogel, K. Hirsch, Klar Ph, et al., Size dependence of $L_{2,3}$ branching ratio and 2p core-hole screening in X-ray absorption of metal clusters, Phys. Rev. Lett. 101 (2008), 153401/1–4.
[51] K. Chen, S. Fiedler, I. Baev, T. Beeck, W. Wurth, M. Martins, Hybridization and magnetism in small FePt alloy clusters, New J. Phys. 14 (2012), 123005/1–10.
[52] G. Akgul, F.A. Akgul, Y. Ufuktepe, Investigation of thickness dependence on electronic structures of iron and nickel thin films by L-edge X-ray absorption spectroscopy, Vacuum 99 (2014) 211–215.
[53] S.J. Sun, H.H. Lin, Diluted magnetic semiconductor at finite temperature, Phys. Lett. A 327 (2004) 73–77.
[54] J.E. Bunder, S.J. Sun, H.H. Lin, Spin-wave relaxation in diluted magnetic semiconductors within the self-consistent Green's function approach, Appl. Phys. Lett. (2006) 89, 072101/1-3.